

Topological Photon Transport in Programmable Photonic Processors via Discretized Evolution of Synthetic Magnetic Fields

Andrea Cataldo^{1,*}, Rohan Yadgirkar¹, Ze-Sheng Xu¹, Govind Krishna¹, Ivan Khaymovich², Val Zwiller¹, Jun Gao^{1,*}, and Ali W. Elshaari^{1,*}

¹Department of Applied Physics, KTH Royal Institute of Technology, Albanova University Centre, Roslagstullsbacken 21, 106 91 Stockholm, Sweden

²Nordita, KTH Royal Institute of Technology and Stockholm University, Hannes Alfvéns väg 11, 106 91 Stockholm, Sweden

*Corresponding authors. Emails: andreacl@kth.se, junga@kth.se, elshaari@kth.se

Abstract

Photons, unlike electrons, do not couple directly to magnetic fields, yet synthetic gauge fields can impart magnetic-like responses and enable topological transport. Discretized Floquet evolution provides a controlled route, where the time-ordered sequencing of non-commuting Hamiltonians imprints complex hopping phases and breaks time-reversal symmetry. However, stabilizing such driven dynamics and observing unambiguous topological signatures on a re-configurable platform has remained challenging. Here we demonstrate synthetic gauge fields for light on a programmable photonic processor by implementing discretized Floquet drives that combine static and dynamic phases. This approach reveals hallmark features of topological transport: chiral circulation that reverses under drive inversion, flux-controlled interference

with high visibility, and robust directional flow stabilized by maximizing the minimal Floquet quasi-energy gap. The dynamics are further characterized by a first-harmonic phase order parameter, whose per-period winding number quantifies angular drift and reverses sign with the drive order. These results establish discretized, gap-optimized Floquet evolution as a versatile and fully programmable framework for topological photonics, providing a compact route to engineer gauge fields, stabilize driven phases, and probe winding-number signatures of chiral transport.

1. Introduction

Magnetic fields profoundly alter the behaviour of charged particles by reshaping their energy spectrum. In two-dimensional electron systems, a perpendicular field condenses continuous bands into a hierarchy of discrete Landau levels, each separated by the cyclotron frequency and hosting a macroscopic degeneracy of states. This quantization underlies the quantum Hall effect, wherein the electrical conductance assumes precisely quantized values. The effect also produces chiral edge states, which are one-way electron channels along material boundaries that are topologically protected against backscattering from disorder [1, 2]. Photons propagate through such magnetic fields unchanged, their spectra unquantized, their transport unprotected. Remarkably, synthetic magnetic fields can induce analogous phenomena in photonic systems, thereby enabling magnetic-like responses and robust optical transport [3–5].

Several approaches have emerged to create these synthetic magnetic fields, broadly following two strategies: structural engineering and temporal modulation. Structural approaches exploit materials that break time-reversal symmetry or geometries that emulate gauge fields while preserving it. Magneto-optical materials provide non-reciprocal light propagation, wherein forward and backward traveling waves experience different phase shifts. Theoretical proposals [6, 7] and microwave demonstrations [8] have validated this approach. At optical frequencies, however, magneto-optical effects become vanishingly weak. Strain-engineered geometries constitute an alternative approach. Carefully designed lattice deformations create spatially varying coupling between optical modes, generating synthetic magnetic fields without magnetic materials. Theoretical work has established that such strain produces photonic Landau levels [9, 10]. These predictions have been confirmed through observations in strained honeycomb lattices [11] and silicon photonic

crystals [12, 13]. Temporal approaches, in contrast, can break reciprocity through harmonic modulation of optical properties. Such modulation targets either the coupling between resonators [14] or refractive index within resonators [15]. Diverse platforms have realized this principle, from optomechanical systems [16] to integrated electro-optic devices [17, 18].

In this work, we demonstrate a photonic quantum simulator of synthetic magnetic fields based on discrete-time evolution. The simulator is implemented on a reconfigurable Mach-Zehnder interferometer (MZI) mesh, which supports arbitrary linear optical transformations [19, 20] and has enabled applications in quantum information processing [21–24], neuromorphic computing [25, 26], and signal processing [27, 28]. We use a Floquet drive in which each period is divided into unitary substeps that sequentially activate selected mode pairs on the MZI mesh while other couplings are held off. The time-ordered product of these steps induces complex hopping phases for photons, realizing a synthetic magnetic flux. Because the substeps do not commute, the evolution depends on their order, which breaks time-reversal symmetry. This programmability allows a single photonic processor to investigate various topological phenomena without separate fabrications by simply adjusting control signals [29, 30]. Leveraging this versatility, we implement three-, four-, and seven-site lattice configurations. Our measurements reveal how each geometry produces distinct magnetic signatures, with the three-site system establishing the fundamental mechanism, the four-site system revealing flux interference, and the seven-site system demonstrating directional photon transport in complex systems.

2. Methods

2.1. Theoretical Framework

The generation of synthetic magnetic fields for photons in our programmable photonic processor relies on the principle of dynamically breaking time-reversal symmetry. This is achieved through a periodic, time-ordered sequence of hopping configurations. As this process constitutes a periodically driven system, its dynamics are described within the framework of Floquet theory.

This principle is best illustrated by analyzing a three-site triangular lattice, for which we define a set of hopping Hamiltonians $\{H_1, H_2, H_3\}$ that activate each edge sequentially:

$$H_1 = J(|1\rangle\langle 2| + |2\rangle\langle 1|), \quad H_2 = J(|2\rangle\langle 3| + |3\rangle\langle 2|), \quad H_3 = J(|3\rangle\langle 1| + |1\rangle\langle 3|), \quad (1)$$

where J is the coupling strength and $|i\rangle$ represents a photon localized at site i . These Hamiltonians cycle with period T , each operating for duration $T/3$ before switching to the next, creating a time-periodic system $H(t) = H(t + T)$. Each subprocess evolves the system through the unitary operator:

$$U_k(T/3) = \exp(-iH_k T/3), \quad k = 1, 2, 3. \quad (2)$$

The Floquet operator, $U_F(T)$, is the time-ordered product of these operators. Consequently, the clockwise (CW) modulation, corresponding to the sequence $H_1 \rightarrow H_2 \rightarrow H_3$, is distinct from its reversed, counter-clockwise (CCW) analogue:

$$U_F^{\text{CW}}(T) = U_3 U_2 U_1, \quad U_F^{\text{CCW}}(T) = U_1 U_2 U_3. \quad (3)$$

For an arbitrary evolution time t , the total unitary operator $U(t)$ can be decomposed based on the number of full driving periods, n , and the residual time, τ , such that $t = nT + \tau$ where $0 \leq \tau < T$. The total evolution operator then takes the form:

$$U(t) = U_{\text{partial}}(\tau)[U_F(T)]^n, \quad (4)$$

where $[U_F(T)]^n$ represents the stroboscopic evolution, and $U_{\text{partial}}(\tau)$ accounts for the incomplete final period. This partial operator is the time-ordered product of the operators U_k that fit within the duration τ . The evolved state is then $|\psi(t)\rangle = U(t)|\psi(0)\rangle$, from the fixed initial state $|\psi(0)\rangle$. This discretized cyclic evolution through the Floquet operator is visualized in Fig. 1.

The time-ordered Floquet drive induces a geometric phase for photons as they hop around the lattice, an effect analogous to the Aharonov-Bohm effect for charged particles in a magnetic field. To see how this emerges, we examine the stroboscopic evolution of the system which by Floquet's theorem can be described by a time-independent effective Hamiltonian H_{eff} defined through:

$$U_F(T) = \exp(-iH_{\text{eff}}T) \quad \Rightarrow \quad H_{\text{eff}} = \frac{i}{T} \ln U_F(T). \quad (5)$$

While the constituent Hamiltonians are real, the non-commuting drive sequence results in an effective Hamiltonian with complex hopping amplitudes:

$$H_{\text{eff}} = \sum_i V_{\text{eff}}^{(i)} |i\rangle \langle i| + \sum_{\langle i,j \rangle} \left(J_{\text{eff}}^{(ij)} e^{i\phi_{ij}} |i\rangle \langle j| + \text{h.c.} \right). \quad (6)$$

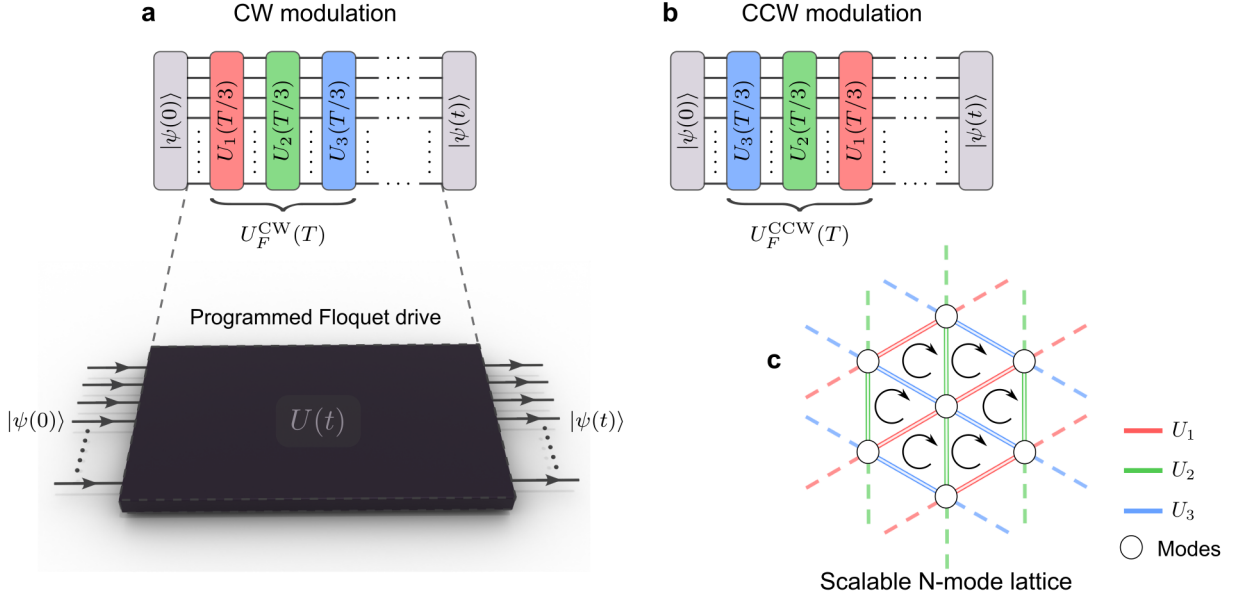


Fig. 1. Discretized Floquet evolution on a programmable photonic processor. A state $|\psi(0)\rangle$ injected on the left bus enters a programmable photonic processor (black box) that implements the time-evolution operator $U(t)$ on N modes, yielding $|\psi(t)\rangle = U(t)|\psi(0)\rangle$ at the right bus. **a**, Clockwise (CW) drive: one period T is decomposed into three sequential substeps $U_1(T/3)$ (red), $U_2(T/3)$ (green), and $U_3(T/3)$ (blue). These time-ordered operations constitute the Floquet operator $U_F^{CW}(T) = U_3 U_2 U_1$. Dashed guide lines indicate that this schedule is programmed onto the chip; horizontal dots indicate repetition over successive periods. At intermediate times (e.g., $t = T/3$), only the substep executed up to that moment has acted. **b**, Counter-clockwise (CCW) drive obtained by reversing the order of the substeps, giving $U_F^{CCW}(T) = U_1 U_2 U_3$. **c**, Scalable N -mode lattice representation. Solid bonds show the coupling pattern active in each substep (colors match panels a–b); dashed bond extensions indicate tiling to larger lattices; white circles mark the modes (waveguides). Curved arrows highlight the induced chiral circulation in each triangular plaquette, illustrating how the programmed drive order generates a synthetic magnetic flux.

Here, $V_{\text{eff}}^{(i)}$ are emergent on-site potentials and J_{eff} are effective coupling strengths. For larger lattices the effective Floquet Hamiltonian is not strictly short-range and, in principle, can include all-to-all terms; it is also not unique for a given $U_F(T)$. The phases ϕ_{ij} can be associated to a synthetic vector potential via:

$$\phi_{ij} = \int_{\mathbf{r}_i}^{\mathbf{r}_j} \mathbf{A} \cdot d\mathbf{l}, \quad (7)$$

with the corresponding synthetic magnetic field $\mathbf{B} = \nabla \times \mathbf{A}$.

In addition to the dynamically programmed phase, $\Phi_{\text{mod}} = \sum \phi_{ij}$, which is set by the modulation timing, we can introduce statically programmed phases, $\Phi_{\text{static}} = \sum_k \alpha_k$, by modifying the hopping terms of the constituent Hamiltonians:

$$H_k = J(e^{i\alpha_k} |i\rangle\langle j| + \text{h.c.}), \quad (8)$$

so that both the dynamic and static contributions combine additively as the total Aharonov-Bohm

phase accumulated in our lattice:

$$\Phi_{\text{total}} = \Phi_{\text{mod}} + \Phi_{\text{static}}. \quad (9)$$

The principle established here can be readily applied to engineer programmable synthetic magnetic fields in larger systems composed of interconnected triangular plaquettes (Fig. 1c).

2.2. Experimental Platform

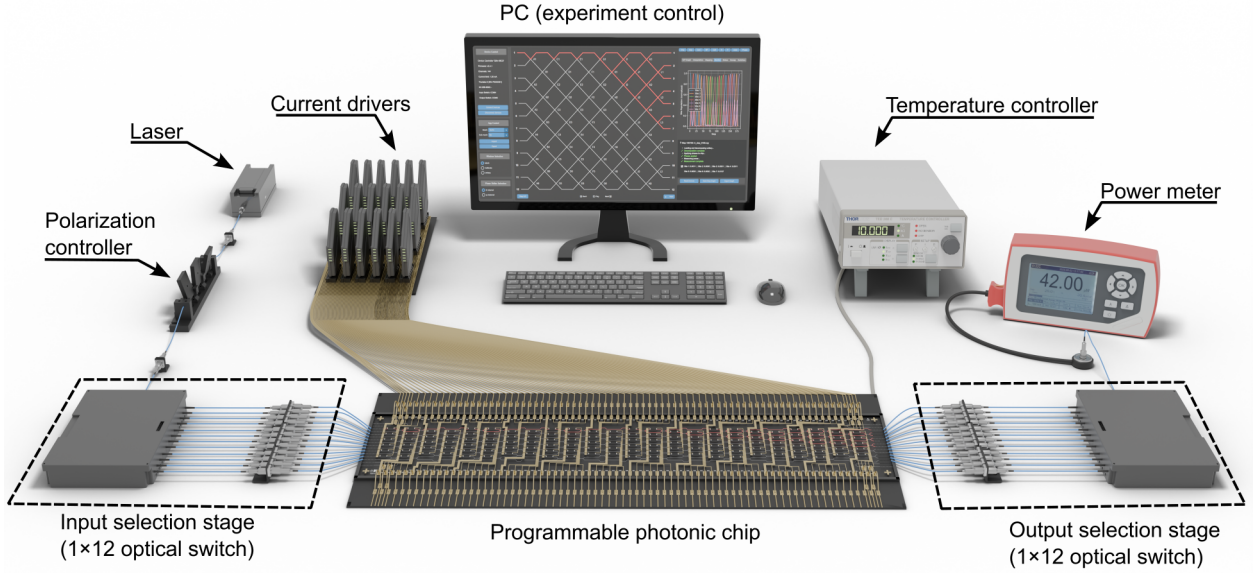


Fig. 2. Experimental setup. Coherent light at 1550 nm from a pulsed diode laser passes through a polarization controller set for TE polarization and is directed to the common port of a 1×12 MEMS optical switch. The switch can be programmed to route the light to any of its twelve multiplexed ports. These ports couple via edge couplers to the corresponding input waveguides of a 12-mode programmable photonic chip, thereby selecting the input. The chip consists of a reconfigurable MZI mesh driven by multichannel current drivers. Light at the chip output is coupled via edge couplers into a second switch operated in reverse; its common port is connected to an optical power meter. Control and acquisition are handled by a PC, which commands the switches, sets the heater currents to realize the unitaries, and logs readings from the power meter. A thermoelectric cooler beneath the chip, regulated by a PID temperature controller, maintains a fixed room-temperature setpoint.

A single programmable photonic chip allowed us to implement three distinct lattice configurations. We first realized a three-site triangular lattice whose single closed loop allowed clear interpretation of directional effects when driving CW and CCW, isolating the non-commuting operations that break time-reversal symmetry. We then programmed a four-site lattice consisting of two coupled triangular lattices with independent phase control. The shared vertices where pathways converge provided observation points for interference effects. Finally, we configured a seven-site

hexagonal lattice to test synthetic magnetic fields in multi-loop geometries. Six perimeter sites surrounding a central node formed a network of interconnected triangular plaquettes, revealing whether directional transport persists in complex systems.

Operating conditions varied across lattice configurations based on their specific requirements. For coherent population transfer in the three-site and four-site systems, we set coupling strengths and evolution times to achieve Rabi π -pulses. This operating point is robust to perturbations in a broad range, given by a finite gap in the corresponding spectrum of the three-site Floquet operator, so the dynamics are tolerant to small period errors as shown in Fig. 5a. While the triangular lattice experiments tested both modulation sequences to establish chirality, the four-site system used only CW driving to focus solely on the interference effects. The seven-site system required a different regime where Rabi pulses are not applicable, so we selected the modulation period by maximizing the minimal quasi-energy gap of the Floquet operator, which yields a stable evolution and robust directional flow. As in the 3-site case, testing both modulation sequences would confirm the presence of the synthetic magnetic field signatures.

The experimental platform, shown in Fig. 2, was based on a photonic chip fabricated at Advanced Micro Foundry using their standard silicon-on-insulator platform with a 220 nm thick silicon layer above a 3 μm buried oxide substrate. It provided 12 input and 12 output waveguide modes interconnected through a reconfigurable mesh of thermally-tuned Mach-Zehnder interferometers controlled by 18 current sources (Qontrol Q8iv, 8 channels each, 740 nA precision). The 500 nm wide waveguides supported single-mode operation in the C-band (1530-1565 nm) with typical propagation losses of 2 dB/cm. Edge couplers at the chip facets allowed fiber-to-chip coupling with losses of approximately 1.3 dB for TE polarization. The chip integrates 264 elements (phase shifters and multimode interferometers). Deep trenches ($280 \times 12 \mu\text{m}$) were included around the MZIs to suppress thermal crosstalk between adjacent heaters. A microscope image of the fabricated photonic chip is shown in Supplementary Fig. S2.

A pulsed diode laser driver (PicoQuant PDL 800-B) operating at 1550 nm provided the coherent light source. The emitted pulses had nominal widths of 50-70 ps FWHM at a repetition frequency of 40 MHz, with an average output power of 3 mW. Light from the laser was coupled to the common port of a 1×12 MEMS fiber optical switch (FiberWDM) via a polarization controller that optimized for TE polarization. The switch directed light to individual chip inputs through PM

fiber connectors at its multiplexed ports. Output signals from the chip were collected through a second identical switch configured in reverse order. Here the common port was connected to an optical power meter (Thorlabs PM100D) equipped with a germanium photodiode sensor (S122C). The sensor operated across 700-1800 nm with a measurement range from 50 nW to 40 mW and a responsivity of approximately 0.96 A/W at 1550 nm. A PC coordinated all instruments, including current control, optical switching, and measurement acquisition, providing full automation of the experiment. Phase relationships in the MZIs were preserved by stabilizing the chip temperature. A thermoelectric cooler beneath the chip, driven by a PID controller (Thorlabs TED200C), maintained temperature stability within $\pm 0.01^\circ\text{C}$. The system used thermistor feedback targeting 10 k Ω (corresponding to room temperature) as its control setpoint.

2.3. Unitary Implementation

We realize the evolution operators from Eqs. (3) by programming the MZI mesh on the photonic chip. Each MZI contains two 3-dB multimode interference couplers and two thermo-optic phase shifters, together implementing a two-mode SU(2) transformation with transfer matrix (Sec. S1):

$$T_{\text{MZI}} = ie^{i\theta/2} \begin{bmatrix} e^{i\varphi} \sin(\theta/2) & \cos(\theta/2) \\ e^{i\varphi} \cos(\theta/2) & -\sin(\theta/2) \end{bmatrix}, \quad (10)$$

where the internal phase shift $\theta \in [0, \pi]$ controls the power splitting ratio between output ports as $\sin^2(\theta/2) : \cos^2(\theta/2)$, and the external phase shift $\varphi \in [0, 2\pi]$ sets their relative phase. Titanium nitride heaters on the upper waveguide arm generate these phase shifts through the thermo-optic effect, with the external heater positioned before the first coupler and the internal heater placed between the two couplers.

Since our theoretical models utilize only a subset of the 12 available modes, we embed the evolution operators into the full-dimensional space. For an n -site lattice with operator U_n acting on selected modes, the embedded 12×12 unitary takes the block-diagonal form:

$$U_{12} = \begin{bmatrix} U_n & 0 \\ 0 & I_{12-n} \end{bmatrix}, \quad (11)$$

where I_{12-n} is the identity matrix for the unused modes. This ensures that light in inactive modes propagates unchanged while lattice dynamics occur exclusively in the active subspace. Physically,

MZIs connecting to unused modes are set to maximum reflectivity $\theta = \pi$, preventing coupling between these modes.

The Clements decomposition [20] expresses this unitary as:

$$U_{12} = D \prod_{(m,n) \in S} T_{m,n}(\theta_{m,n}, \varphi_{m,n}), \quad (12)$$

where D represents diagonal phase factors at the output ports, S denotes the ordered sequence of mode pairs, and each $T_{m,n}$ is the 12×12 matrix with the 2×2 block from Eq. (10) acting on modes m and n . Applying this decomposition to our embedded evolution operators yielded the set of phase values $\{(\theta_{m,n}, \varphi_{m,n})\}$ that parametrize each MZI on the chip.

Realizing these target phase shifts from the unitary decomposition requires compensating for phase variations in each MZI through systematic calibration. The full characterization and fitting procedure for the current-phase relation is provided in the Supplementary Materials (Sec. S2).

2.4. Data Acquisition and Analysis

We measured the transient population dynamics by applying the unitaries incrementally rather than as single operations. This allowed us to resolve intermediate dynamics throughout the modulation cycle. Each period T was divided into 60 steps where 20 steps were allocated to each subprocess (U_1, U_2, U_3).

The measurement procedure began with state preparation using the input fiber switch set to the first port of the mesh. For the three-site and seven-site lattices, we initialized the system with unit population at site 1, implementing the state $|1\rangle$. The four-site system required the symmetric superposition $(|1\rangle + |3\rangle)/\sqrt{2}$, which we prepared using two sequential MZIs to route equal portions of the input light to modes 1 and 3.

For each discretized time step, we decomposed the corresponding unitary operator and applied the resulting phase shifts to the mesh. The current drivers set the required heater currents, with a 1-second dwell time ensuring thermal steady state before measurement. The initial state remained fixed throughout the evolution, with each unitary step representing the cumulative evolution from $t = 0$ to the current time.

Output power measurements proceeded systematically across all active modes. The fiber switch automatically cycled through the output ports corresponding to the lattice sites, with a 50 ms switching delay ensuring mechanical stability. The optical power meter recorded the transmitted

power at each port with hardware averaging of 20 samples. We treated each raw reading as having a $\pm 3\%$ relative uncertainty.

To account for variations in fiber-to-chip coupling efficiency, we normalized the measured powers at each time step. The population at site i was calculated as:

$$P_i = \frac{P_{i,\text{raw}}}{\sum_j P_{j,\text{raw}}}, \quad (13)$$

where $P_{i,\text{raw}}$ denotes the raw measured power at site i and the sum extends over all active lattice sites. Assuming independent channel errors with $\sigma(P_{j,\text{raw}}) = r P_{j,\text{raw}}$, the corresponding 1σ uncertainty on the normalized populations was obtained by standard error propagation:

$$\sigma(P_i) = r P_i \sqrt{1 + \sum_j P_j^2 - 2P_i}, \quad r = 0.03, \quad (14)$$

and we report $P_i \pm \sigma(P_i)$ throughout.

3. Results

3.1. Minimal geometry for synthetic magnetic fields

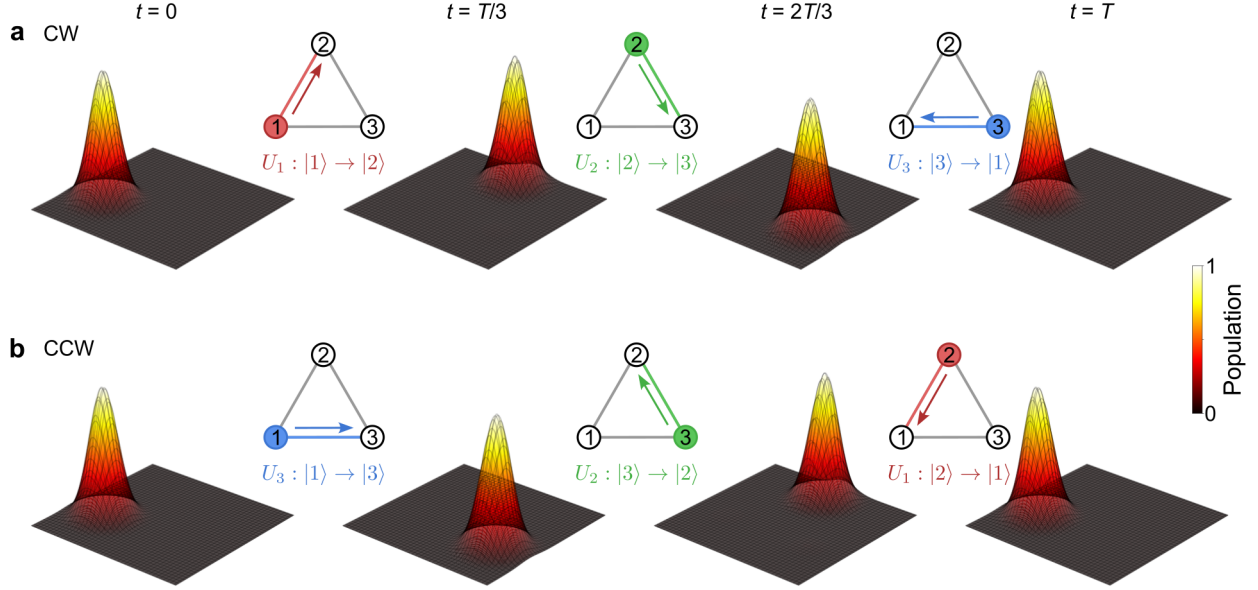


Fig. 3. Chiral photon transport in a three-site plaquette. Each row shows four snapshots of the system's state, taken at the switching boundaries $t = 0, T/3, 2T/3$ and T . For every snapshot, the colored surface represents the experimental normalized population, rendered as a single smooth surface by summing three Gaussian peaks centered at the lattice sites. The black wireframe overlays the simulated population. In the triangular schematics, a colored bond marks the active substep, with $U_1(T/3)$ red, $U_2(T/3)$ green, and $U_3(T/3)$ blue. The arrow direction indicates the transport directionality, and gray bonds are off. **a**, For clockwise (CW) modulation, the population transfers sequentially along the path $1 \rightarrow 2 \rightarrow 3 \rightarrow 1$. **b**, For counter-clockwise (CCW) modulation, the sequence reverses to $1 \rightarrow 3 \rightarrow 2 \rightarrow 1$. The close surface-wireframe overlap indicates excellent agreement. Reversing the drive clearly reverses the circulation.

Fig. 3 presents snapshots of the population dynamics for a system initialized with unit population at site 1. The evolution spans one complete modulation period T . Under CW modulation (Fig. 3a), the evolution according to Eq. (3) drives coherent population transfer along the path $1 \rightarrow 2 \rightarrow 3 \rightarrow 1$. The system operates with Rabi π -pulses ($JT/3 = \pi/2$) to ensure complete transfer between coupled sites. Simulation results reveal near-perfect sequential transfer at the expected times. Experimental measurements yield fidelities of $99.05 \pm 0.04\%$, $99.09 \pm 0.04\%$, and $99.70 \pm 0.01\%$.

CCW modulation (Fig. 3b) implements the reversed evolution according to Eq. (3), driving population along $1 \rightarrow 3 \rightarrow 2 \rightarrow 1$. Both simulation and experiment demonstrate comparable

efficiency, with fidelities of $99.57 \pm 0.02\%$, $98.47 \pm 0.06\%$, and $99.78 \pm 0.01\%$. The opposite circulation patterns generate artificial magnetic fluxes of opposite signs, directly confirming time-reversal symmetry breaking in our programmable platform.

We also note that the observed circulation depends on the choice of initialization site. Starting from site 1 produces one-period CW/CCW cycles as demonstrated. If instead the system is prepared on site 2 or 3, the population moves only every other substep, so the effective circulation appears reversed and closes only after two periods.

3.2. Flux-steered interferometry in a two-plaquette lattice

The next step extends the single triangle to a pair of triangular plaquettes that share an edge, forming a two-path interferometer configuration. Both plaquettes are driven in parallel by the same CW three-step sequence U_1, U_2, U_3 with period $T = 3\pi/(2J)$. Static phases are programmed on the outer bonds in the form of Eq. (8), which sets loop phases Φ_A and Φ_B around plaquettes A and B. Because the modulation-induced phase Φ_{mod} from the CW drive is common to both loops, the observable that steers interference at the shared vertices is the synthetic flux difference:

$$\Delta\Phi \equiv \Phi_A - \Phi_B, \quad (15)$$

consistent with the additive structure in Eq. (9) where the common modulation contribution cancels in the difference.

Fig. 4 presents the implementation and readout of this interferometer. Panel **a** shows the lattice schematic (sites 1-4) where bonds are color-coded to the three substeps of the CW drive (U_1 red, U_2 green on the shared edge, and U_3 blue). The circular arrows label the net loop phases Φ_A and Φ_B around the left and right triangles; individual bond phases are not depicted. The input is prepared in the symmetric superposition $(|1\rangle + |3\rangle)/\sqrt{2}$ so that amplitudes launch into both loops. During one drive period T , the sequence in Eq. (3) routes these amplitudes to the shared sites 2 and 4 where they interfere. With this initial state, reversing the drive order yields indistinguishable populations at the shared sites, so the protocol's time-reversal symmetry breaking is obscured in this configuration. Using a different input, such as adding a relative phase between $|1\rangle$ and $|3\rangle$, would reveal the driving direction. Here we focus on the interferometric response.

The resulting interference is shown in panel **b** as the simulated mid-period populations $P_2(T/2)$ and $P_4(T/2)$ as $\Delta\Phi$ is swept. The two traces are complementary and cross at $\Delta\Phi = 0$,

where the populations are balanced. This follows from a two-path picture. During U_2 the fields at the shared sites are coherent sums of the amplitudes from the two plaquettes that differ only by the programmed flux difference. With the phase origin chosen so that $\Delta\Phi = 0$ yields equal populations, the dependence is consistent with:

$$P_{2,4}(T/2) = \frac{1}{2}[1 \pm V \sin(\Delta\Phi/2)], \quad (16)$$

where $0 \leq V \leq 1$ is the visibility, the upper sign corresponds to site 2, and the lower to site 4. This form explains the smooth S-shaped exchange of population and the complementarity $P_2 + P_4 = 1$.

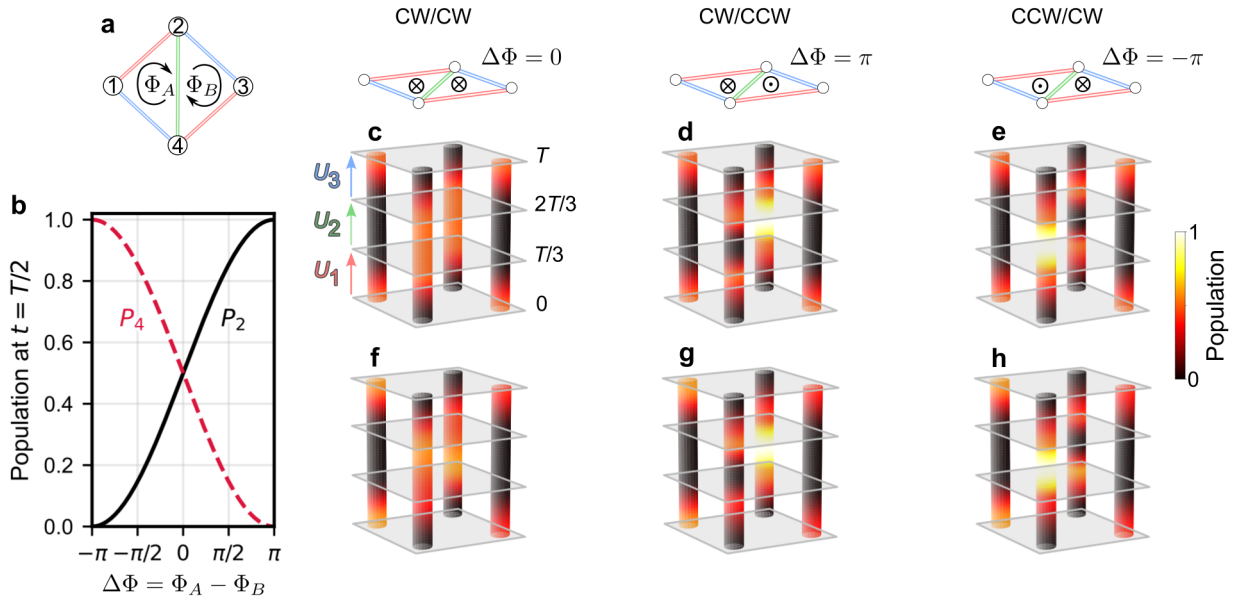


Fig. 4. Flux-tuned interference in a four-site lattice. **a**, Schematic of two triangles A and B with a shared edge (green), driven by the CW sequence U_1 (red), U_2 (green), and U_3 (blue). Triangles A and B have loop fluxes Φ_A and Φ_B , respectively. Interference at the shared vertices (sites 2 and 4) is governed by their flux difference $\Delta\Phi \equiv \Phi_A - \Phi_B$. The initial state is $(|1\rangle + |3\rangle)/\sqrt{2}$, launching light into both loops. **b**, Simulated mid-period ($t = T/2$) populations P_2 (black) and P_4 (red, dashed) versus $\Delta\Phi$; the traces are complementary and cross at $\Delta\Phi = 0$. **c-e**, Simulated dynamics over one period $t = T$ for $\Delta\Phi = 0$ (CW/CW), $+\pi$ (CW/CCW), and $-\pi$ (CCW/CW). Horizontal planes mark $t = 0, T/3, 2T/3, T$ and the colored labels indicate the active substep U_1, U_2, U_3 between planes. Insets use \otimes/\odot to denote flux into/out of the triangle plane (drawn above population columns). **f-h**, Measured dynamics for the same settings, showing balanced splitting at $\Delta\Phi = 0$, constructive interference at site 2 for $+\pi$, and at site 4 for $-\pi$, in agreement with simulations. In the latter two cases, destructive interference suppresses the green link, so the effective dynamics proceed primarily through the red and blue couplings. Color scale indicates normalized population.

Panels **c-e** display simulated population dynamics for three representative settings of $\Delta\Phi$. For $\Delta\Phi = 0$ (CW/CW in the relative sense), the amplitudes from the two loops arrive in phase, distributing populations equally at sites 2 and 4 at the mid-period. Shifting to $\Delta\Phi = +\pi$ (CW/CCW)

reverses the relative sign of one path, so that constructive interference occurs at site 2 while destructive interference suppresses site 4. Reversing the sign to $\Delta\Phi = -\pi$ flips the pattern, brightening site 4 and dimming site 2.

Panels **f-h** present the measurements. As $\Delta\Phi$ is tuned from 0 to $+\pi$ and then to $-\pi$, the population shifts between the two shared sites in agreement with the simulations. At the mid-period, the balanced case ($\Delta\Phi = 0$) yields $P_2 = 50.29 \pm 1.05\%$ and $P_4 = 48.73 \pm 1.05\%$. A relative shift of $+\pi$ favors site 2 ($96.77 \pm 0.11\%$) while suppressing site 4 ($2.03 \pm 0.08\%$), and reversing the sign inverts the distribution, with site 4 at $98.28 \pm 0.06\%$ and site 2 at $0.73 \pm 0.03\%$.

3.3. Directional transport in a multi-plaquette hexagonal lattice

We now scale to a geometry where intertwined loops come together in a seven-site hexagon surrounding a central site. In the three-site and four-site lattices each step of the drive couples only two sites, so the evolution follows simple two-level dynamics with complete transfer via Rabi π -pulses. This clear condition no longer applies in lattices where a driving step may couple more than two sites, which breaks the isolated two-level picture and makes the effective Floquet Hamiltonian long-ranged. We therefore identify stable operating points by examining the quasi-energy spectrum of the Floquet operator U_F . Its eigenvalues take the form $\lambda_k = e^{-i\varepsilon_k T}$, where the quasi-energies satisfy $0 \leq \varepsilon_k < 2\pi/T$. The stability of the dynamics is set by separation between the quasi-energies. We define the minimal splitting:

$$\Delta\varepsilon_{\min} = \min_{i \neq j} |\varepsilon_i - \varepsilon_j|, \quad (17)$$

which quantifies the smallest gap in the spectrum (distance measured mod $2\pi/T$ on a circle).

In any physical implementation the ideal operator $U_F(T)$ is subject to small, random perturbations in control parameters (e.g. heater currents), leading to an implemented operator:

$$U_{\text{actual}}(T) = U_F(T) + \delta U, \quad (18)$$

where δU is a random matrix representing the integrated effect of experimental imperfections over one period. A small gap ($\Delta\varepsilon_{\min} \rightarrow 0$) indicates a near-degeneracy where the system's final state becomes highly sensitive to δU , causing the states to mix unpredictably. A larger gap corresponds to a more stable, well-separated evolution, which ensures the evolution is robust against such

perturbations. Our strategy is therefore to find the optimal period, T_{opt} , that maximizes this gap:

$$T_{\text{opt}} = \arg \max_T [\Delta \varepsilon_{\min}(T)]. \quad (19)$$

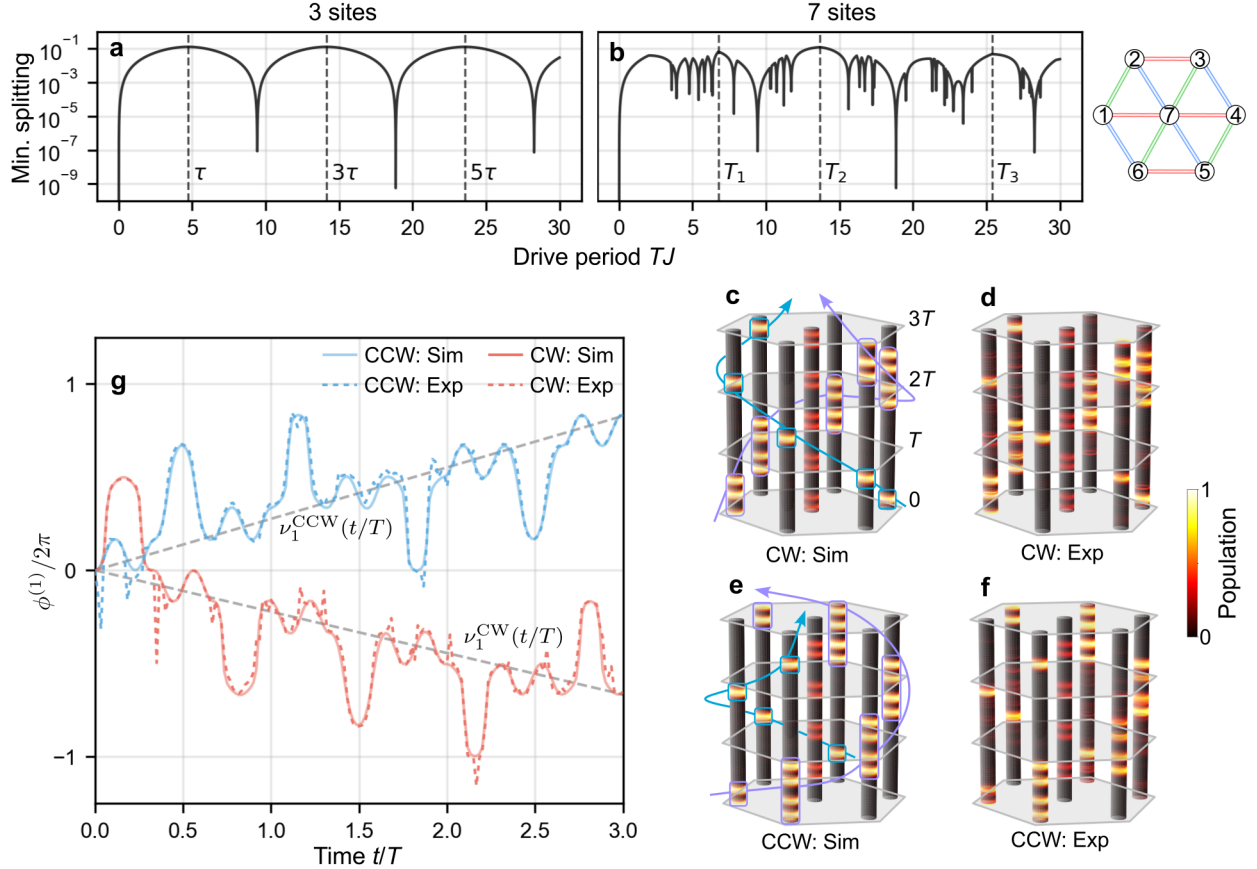


Fig. 5. Floquet-period optimization and directional transport in a seven-site hexagon. Top-right: schematic of the lattice with color-coded bonds (red/green/blue for $U_1/U_2/U_3$). The system is initialized in state $|1\rangle$. **a**, Minimal quasi-energy splitting $\Delta \varepsilon_{\min}$ of the three-site Floquet operator $U_F(T)$ versus drive period T (dimensionless; $J = \hbar = 1$). Peaks at τ , 3τ , 5τ mark the Rabi π condition and its odd multiples with the maximum splitting reaching $\Delta \varepsilon_{\min} = 0.125$. The dips indicate near-degeneracy of quasi-energies. **b**, In the seven-site case, operating points are identified at $T_1 = 6.7574$, $T_2 = 13.6647$ (used in sim/exp, $\Delta \varepsilon_{\min} = 0.119$), and $T_3 = 25.3791$. **c,d**, CW modulation: simulated and experimental population dynamics over three driving periods ($t = 3T$). Oscillatory exchanges are observed within each substep with an overall CW circulation. Violet boxes mark the multi-peak packet and cyan boxes the single-peak packet, with an overlaid arrow indicating the trajectory; these two contributions form a superposition and both advance in the CW sense. **e,f**, For CCW modulation, the circulation reverses: the same guides show the multi-peak and single-peak packets advancing CCW. **g**, First harmonic Fourier phase $\phi^{(1)}/2\pi$, defined in Eq. (21), from the measured and simulated dynamics. Solid (sim) and dashed (exp) are overlaid. Gray guide lines with slopes $\nu_1^{\text{CCW}} = 0.276$ and $\nu_1^{\text{CW}} = -0.222$ indicate the extracted per-period winding numbers. Traces show opposite overall trends for CW (red) versus CCW (blue), consistent with broken time-reversal symmetry. Movies of evolutions are provided in the Supplementary Materials.

To validate the period-selection procedure, we first applied it to the 3-site lattice. The

results, shown in Fig. 5a, reveal a periodic spectrum of stability peaks. Notably, one of these peaks at $T = 4.7109$ coincides with the familiar π -pulse condition, while the subsequent peaks represent its odd multiples, where a complete state transfer also occurs. This confirms our method correctly identifies the entire family of known coherent evolution points, each corresponding to a non-degenerate system with a minimal splitting of $\Delta\varepsilon_{\min} = 0.125$.

We then evaluated the seven-site hexagon (Fig. 5b). Although more complex, the system retains features of the 3-site lattice, including the shared near-degeneracy locations. An optimal peak $T_{\text{opt}} = 13.6647$ was selected for the experiment, which occurs near a stability peak of its underlying 3-site building block $T = 14.1388$. Consequently, the seven quasi-energies arrange themselves into a near-uniform, maximally gapped configuration ($\Delta\varepsilon_{\min} = 0.119$).

The seven-site hexagonal lattice presents qualitatively different behavior from our minimal configurations. Fig. 5(c-f) shows population dynamics over three modulation periods $t = 3T$, demonstrating oscillatory exchange between coupled sites superimposed on global directional flow. These oscillations migrate around the hexagon with each Hamiltonian switch, producing a clear rotating pattern that follows the modulation direction throughout the evolution. The drive produces sequential site occupations with high population transfer at various stages, while the central site (7) acts mainly as a transient hub and remains only weakly populated overall. The clockwise case is shown in Fig. 5(c,d) and the counterclockwise case in Fig. 5(e,f), where reversing the drive order flips the direction of the rotating pattern. Extended $9T$ dynamics showing more than one full rotation are provided in Supplementary Sec. S4.

As a complementary view of the transport, Fig. 5g shows the first-harmonic Fourier phase extracted from the measured and simulated populations. Assign each site an azimuthal angle θ_k according to the lattice geometry (with the central site taken as $\theta_7 = 0$), and the complex first-harmonic is formed as:

$$C^{(1)}(t) = \sum_{k=1}^7 P_k(t) e^{i\theta_k}, \quad (20)$$

where $P_k(t)$ is the population at site k . Its phase:

$$\phi^{(1)}(t) = \arg[C^{(1)}(t)], \quad (21)$$

provides a measure of the net angular drift and is expected to have an overall linear growth. Expressed in cycles (i.e., $\phi^{(1)}/2\pi$), the phase drifts nearly linearly over the periods; the slope's sign

sets the transport direction, and small kinks appear when population transiently occupies the central site, pulling $C^{(1)}(t)$ toward $\theta = 0$. We quantify this drift by an empirical per-period winding number, $\nu_1 \equiv \frac{1}{2\pi} \frac{d\phi^{(1)}}{d(t/T)}$, i.e., the slope of $\phi^{(1)}/2\pi$ versus t/T . From Fig. 5g we obtain $\nu_1^{\text{CW}} = -0.222$ and $\nu_1^{\text{CCW}} = +0.276$, with the sign reversing under drive inversion. The experimental traces follow closely (correlation $r = 0.989$ for CW; $r = 0.985$ for CCW). While the seven-site, open system does not enforce quantization, the nonzero and sign-robust ν_1 is consistent with a nontrivial per-period phase winding and the observed chiral transport.

4. Conclusion

In this work, we have demonstrated that discretized Floquet evolution on a programmable photonic processor provides a powerful and highly flexible method for generating synthetic gauge fields. By systematically breaking time-reversal symmetry with time-ordered coupling sequences, we validated the core principles of this approach, progressing from the demonstration of fundamental chiral transport in a single plaquette to coherent, flux-controlled routing in an interferometric geometry, and finally to directional transport in a complex multi-loop lattice. This technique moves beyond static, fabrication-defined implementations by offering a fully programmable route to engineer complex Hamiltonians and explore a wide range of topological phenomena on a single chip.

References

- [1] D. J. Thouless, M. Kohmoto, M. P. Nightingale, and M. den Nijs, “Quantized hall conductance in a two-dimensional periodic potential,” *Phys. Rev. Lett.*, vol. 49, pp. 405–408, Aug 1982.
- [2] B. I. Halperin, “Quantized hall conductance, current-carrying edge states, and the existence of extended states in a two-dimensional disordered potential,” *Phys. Rev. B*, vol. 25, pp. 2185–2190, Feb 1982.
- [3] R. O. Umucalılar and I. Carusotto, “Artificial gauge field for photons in coupled cavity arrays,” *Physical Review A*, vol. 84, no. 4, Oct. 2011.

- [4] K. Fang, Z. Yu, and S. Fan, “Photonic aharonov-bohm effect based on dynamic modulation,” *Phys. Rev. Lett.*, vol. 108, p. 153901, Apr 2012.
- [5] M. Hafezi, S. Mittal, J. Fan, A. Migdall, and J. M. Taylor, “Imaging topological edge states in silicon photonics,” *Nature Photonics*, vol. 7, no. 12, p. 1001–1005, Oct. 2013.
- [6] F. D. M. Haldane and S. Raghu, “Possible realization of directional optical waveguides in photonic crystals with broken time-reversal symmetry,” *Phys. Rev. Lett.*, vol. 100, p. 013904, Jan 2008.
- [7] S. Raghu and F. D. M. Haldane, “Analogues of quantum-hall-effect edge states in photonic crystals,” *Phys. Rev. A*, vol. 78, p. 033834, Sep 2008.
- [8] Z. Wang, Y. Chong, J. D. Joannopoulos, and M. Soljačić, “Observation of unidirectional backscattering-immune topological electromagnetic states,” *Nature*, vol. 461, no. 7265, pp. 772–775, 2009.
- [9] M. C. Rechtsman, J. M. Zeuner, A. Tünnermann, S. Nolte, M. Segev, and A. Szameit, “Strain-induced pseudomagnetic field and photonic landau levels in dielectric structures,” *Nature Photonics*, vol. 7, no. 2, pp. 153–158, 2013.
- [10] J. Guglielmon, M. C. Rechtsman, and M. I. Weinstein, “Landau levels in strained two-dimensional photonic crystals,” *Phys. Rev. A*, vol. 103, p. 013505, Jan 2021.
- [11] O. Jamadi, E. Rozas, G. Salerno, M. Milićević, T. Ozawa, I. Sagnes, A. Lemaître, L. Le Gratiet, A. Harouri, I. Carusotto, J. Bloch, and A. Amo, “Direct observation of photonic landau levels and helical edge states in strained honeycomb lattices,” *Light: Science & Applications*, vol. 9, no. 1, p. 144, 2020.
- [12] R. Barczyk, L. Kuipers, and E. Verhagen, “Observation of landau levels and chiral edge states in photonic crystals through pseudomagnetic fields induced by synthetic strain,” *Nature Photonics*, vol. 18, no. 6, pp. 574–579, 2024.
- [13] M. Barsukova, F. Gris , Z. Zhang, S. Vaidya, J. Guglielmon, M. I. Weinstein, L. He, B. Zhen, R. McEntaffer, and M. C. Rechtsman, “Direct observation of landau levels in silicon photonic crystals,” *Nature Photonics*, vol. 18, no. 6, pp. 580–585, 2024.

- [14] K. Fang, Z. Yu, and S. Fan, “Realizing effective magnetic field for photons by controlling the phase of dynamic modulation,” *Nature Photonics*, vol. 6, no. 11, pp. 782–787, 11 2012.
- [15] L. D. Tzuang, K. Fang, P. Nussenzveig, S. Fan, and M. Lipson, “Non-reciprocal phase shift induced by an effective magnetic flux for light,” *Nature Photonics*, vol. 8, no. 9, pp. 701–705, 9 2014.
- [16] M. Schmidt, S. Kessler, V. Peano, O. Painter, and F. Marquardt, “Optomechanical creation of magnetic fields for photons on a lattice,” *Optica*, vol. 2, no. 7, pp. 635–641, Jul 2015.
- [17] A. Dutt, Q. Lin, L. Yuan, M. Minkov, M. Xiao, and S. Fan, “A single photonic cavity with two independent physical synthetic dimensions,” *Science*, vol. 367, no. 6473, pp. 59–64, 2020.
- [18] H. X. Dinh, A. Balčytis, T. Ozawa, Y. Ota, G. Ren, T. Baba, S. Iwamoto, A. Mitchell, and T. G. Nguyen, “Reconfigurable synthetic dimension frequency lattices in an integrated lithium niobate ring cavity,” *Communications Physics*, vol. 7, no. 1, p. 185, 6 2024.
- [19] M. Reck, A. Zeilinger, H. J. Bernstein, and P. Bertani, “Experimental realization of any discrete unitary operator,” *Phys. Rev. Lett.*, vol. 73, pp. 58–61, Jul 1994.
- [20] W. R. Clements, P. C. Humphreys, B. J. Metcalf, W. S. Kolthammer, and I. A. Walmsley, “Optimal design for universal multiport interferometers,” *Optica*, vol. 3, no. 12, pp. 1460–1465, Dec 2016.
- [21] J. Carolan, C. Harrold, C. Sparrow, E. Martín-López, N. J. Russell, J. W. Silverstone, P. J. Shadbolt, N. Matsuda, M. Oguma, M. Itoh *et al.*, “Universal linear optics,” *Science*, vol. 349, no. 6249, pp. 711–716, 2015.
- [22] X. Qiang, X. Zhou, J. Wang, C. M. Wilkes, T. Loke, S. O’Gara, L. Kling, G. D. Marshall, R. Santagati, T. C. Ralph, J. B. Wang, J. L. O’Brien, M. G. Thompson, and J. C. F. Matthews, “Large-scale silicon quantum photonics implementing arbitrary two-qubit processing,” *Nature Photonics*, vol. 12, no. 9, pp. 534–539, 9 2018.
- [23] S. Paesani, Y. Ding, R. Santagati, L. Chakhmakhchyan, C. Vigliar, K. Rottwitt, L. K. Oxenløwe, J. Wang, M. G. Thompson, and A. Laing, “Generation and sampling of quantum states of light in a silicon chip,” *Nature Physics*, vol. 15, no. 9, pp. 925–929, 9 2019.

- [24] J. Wang, F. Sciarrino, A. Laing, and M. G. Thompson, “Integrated photonic quantum technologies,” *Nature Photonics*, vol. 14, no. 5, pp. 273–284, 5 2020.
- [25] Y. Shen, N. C. Harris, S. Skirlo, M. Prabhu, T. Baehr-Jones, M. Hochberg, X. Sun, S. Zhao, H. Larochelle, D. Englund, and M. Soljačić, “Deep learning with coherent nanophotonic circuits,” *Nature Photonics*, vol. 11, no. 7, pp. 441–446, 7 2017.
- [26] B. J. Shastri, A. N. Tait, T. Ferreira de Lima, W. H. P. Pernice, H. Bhaskaran, C. D. Wright, and P. R. Prucnal, “Photonics for artificial intelligence and neuromorphic computing,” *Nature Photonics*, vol. 15, no. 2, pp. 102–114, 2 2021.
- [27] D. Pérez, I. Gasulla, L. Crudgington, D. J. Thomson, A. Z. Khokhar, K. Li, W. Cao, G. Z. Mashanovich, and J. Capmany, “Multipurpose silicon photonics signal processor core,” *Nature Communications*, vol. 8, no. 1, p. 636, 9 2017.
- [28] D. Marpaung, J. Yao, and J. Capmany, “Integrated microwave photonics,” *Nature Photonics*, vol. 13, no. 2, pp. 80–90, 2 2019.
- [29] N. C. Harris, G. R. Steinbrecher, M. Prabhu, Y. Lahini, J. Mower, D. Bunandar, C. Chen, F. N. C. Wong, T. Baehr-Jones, M. Hochberg, S. Lloyd, and D. Englund, “Quantum transport simulations in a programmable nanophotonic processor,” *Nature Photonics*, vol. 11, no. 7, pp. 447–452, 7 2017.
- [30] W. Bogaerts, D. Pérez, J. Capmany, D. A. B. Miller, J. Poon, D. Englund, F. Morichetti, and A. Melloni, “Programmable photonic circuits,” *Nature*, vol. 586, no. 7828, pp. 207–216, 10 2020.
- [31] C. Alexiev, J. C. C. Mak, W. D. Sacher, and J. K. S. Poon, “Calibrating rectangular interferometer meshes with external photodetectors,” *OSA Continuum*, vol. 4, no. 11, pp. 2892–2904, Nov 2021.
- [32] S. Lin, Y. Zhang, Z. Wu, S. Zeng, Q. Gao, J. Li, X. Yu, and S. Yu, “Power-efficient programmable integrated multiport photonic interferometer in cmos-compatible silicon nitride,” *Photonics Research*, vol. 12, no. 11, p. A11, 3 2024.

Acknowledgments: A.C., Z.Xu, G.K and A.W.E acknowledges the support from Knut and Alice Wallenberg (KAW) Foundation through the Wallenberg Centre for Quantum Technology (WACQT). J.G. acknowledges support from Swedish Research Council (Ref: 2023-06671 and 2023-05288), Vinnova project (Ref: 2024-00466) and the Göran Gustafsson Foundation. A.W.E acknowledges support from Swedish Research Council (VR) Starting Grant (Ref: 2016-03905). V.Z. acknowledges support from the KAW. I. M. K. acknowledges support by the European Research Council under the European Union’s Seventh Framework Program Synergy ERC-2018-SyG HERO-810451.

Author contributions: A.C. performed the experiments, simulations, data analysis, and manuscript drafting. I.K. and A.W.E conceived the idea. A.C., R.Y., and Z.-S.X. developed the experimental platform. G.K. contributed to discussions on the unitary decomposition algorithm and calibration procedure. I.K., J.G., and A.W.E. discussed the results and contributed to the manuscript. A.W.E. and J.G. supervised the project. V.Z. provided input on the manuscript.

Competing interests: The authors declare no competing financial interests

Data and materials availability: The authors agree to make any data necessary to support or replicate the claims made in this article available upon reasonable request.

Supplementary Materials

S1. MZI Transfer Matrix Derivation

The transfer matrix for the Mach-Zehnder interferometer (MZI) used in this work is derived here. The MZI consists of four components in series: an external phase shifter φ , a first 3-dB ideal coupler, an internal phase shifter θ , and a second 3-dB ideal coupler (Fig. S1).

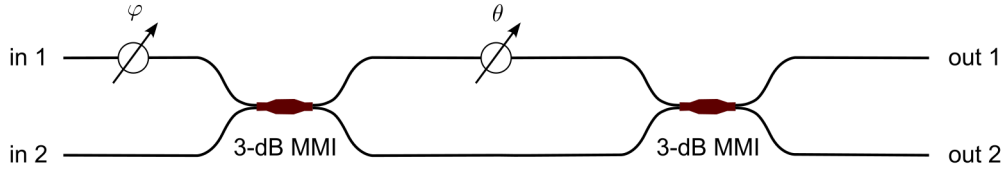


Fig. S1. Schematic of a Mach-Zehnder interferometer (MZI) composed of two 3-dB MMIs and two thermo-optic phase shifters (φ, θ). Inputs and outputs labeled in 1–2, out 1–2.

The transfer matrices for the phase shifters and the ideal 3-dB coupler are defined as:

$$T_{\varphi} = \begin{bmatrix} e^{i\varphi} & 0 \\ 0 & 1 \end{bmatrix}, \quad T_{\theta} = \begin{bmatrix} e^{i\theta} & 0 \\ 0 & 1 \end{bmatrix}, \quad T_C = \frac{1}{\sqrt{2}} \begin{bmatrix} 1 & i \\ i & 1 \end{bmatrix}. \quad (\text{S1})$$

The total transfer matrix is the product of these individual components:

$$T_{\text{MZI}} = T_C T_{\theta} T_C T_{\varphi} \quad (\text{S2})$$

$$\begin{aligned} &= \left(\frac{1}{\sqrt{2}} \begin{bmatrix} 1 & i \\ i & 1 \end{bmatrix} \begin{bmatrix} e^{i\theta} & 0 \\ 0 & 1 \end{bmatrix} \right) \left(\frac{1}{\sqrt{2}} \begin{bmatrix} 1 & i \\ i & 1 \end{bmatrix} \begin{bmatrix} e^{i\varphi} & 0 \\ 0 & 1 \end{bmatrix} \right) \\ &= \frac{1}{2} \begin{bmatrix} e^{i\varphi}(e^{i\theta} - 1) & i(e^{i\theta} + 1) \\ ie^{i\varphi}(e^{i\theta} + 1) & 1 - e^{i\theta} \end{bmatrix}. \end{aligned} \quad (\text{S3})$$

Using the identities $e^{i\theta} - 1 = 2i \sin(\theta/2)e^{i\theta/2}$ and $e^{i\theta} + 1 = 2 \cos(\theta/2)e^{i\theta/2}$, leads to the final result:

$$T_{\text{MZI}} = ie^{i\theta/2} \begin{bmatrix} e^{i\varphi} \sin(\theta/2) & \cos(\theta/2) \\ e^{i\varphi} \cos(\theta/2) & -\sin(\theta/2) \end{bmatrix}. \quad (\text{S4})$$

S2. Phase Shifter Calibration

Accurate realization of the unitary transformations requires calibrating the thermo-optic phase shifters in each MZI. The total phase accumulated in each MZI consists of both an electrically-controlled contribution and a fabrication-induced static offset:

$$\alpha_{\text{total}}(I) = \alpha_{\text{elec}}(I) + \alpha_{\text{static}}, \quad (\text{S5})$$

where α represents either θ or φ and I is the applied current.

We empirically find that the heater voltage follows $V = aI^3 + cI + d$, indicating a temperature-dependent resistance $R(I) = aI^2 + c$ arising from the resistivity increase with heating. The dissipated power $P = I^2 R(I)$ induces a phase shift through:

$$\alpha_{\text{total}}(I) = \beta(aI^4 + cI^2) + \alpha_{\text{static}}, \quad (\text{S6})$$

where β is the thermo-optic efficiency coefficient.

We characterize each MZI through two sequential measurements. First, we perform resistance characterization with current-voltage measurements from 0 to 1.35 mA in 10 steps, extracting coefficients a , c , and d . Second, we route light exclusively through the target MZI and measure transmitted optical power while sweeping the current in 50 steps. Using the resistance model from the first measurement, we calculate the heating power at each current and space these measurements uniformly in power. The optical power follows a sinusoidal modulation with heating power:

$$P_{\text{out}} = P_{\text{avg}}[1 \pm \cos(\omega P_{\text{heat}} + \phi_0)], \quad (\text{S7})$$

where $P_{\text{heat}} = aI^4 + cI^2$ and the sign (\pm) depends on the measurement configuration, with opposite input-output ports giving the cross configuration (+) and the same ports giving the bar configuration (-). Fitting this response yields $\omega = \beta$ and $\phi_0 = \alpha_{\text{static}}$, enabling the calculation of the required current for any target phase through numerical solution of Eq. (S6).

This fitting procedure applies to both internal and external phase shifters. While internal phases require routing light exclusively through individual MZIs [31], external phases require extended interferometric configurations for characterization [32].

S3. Photonic chip image

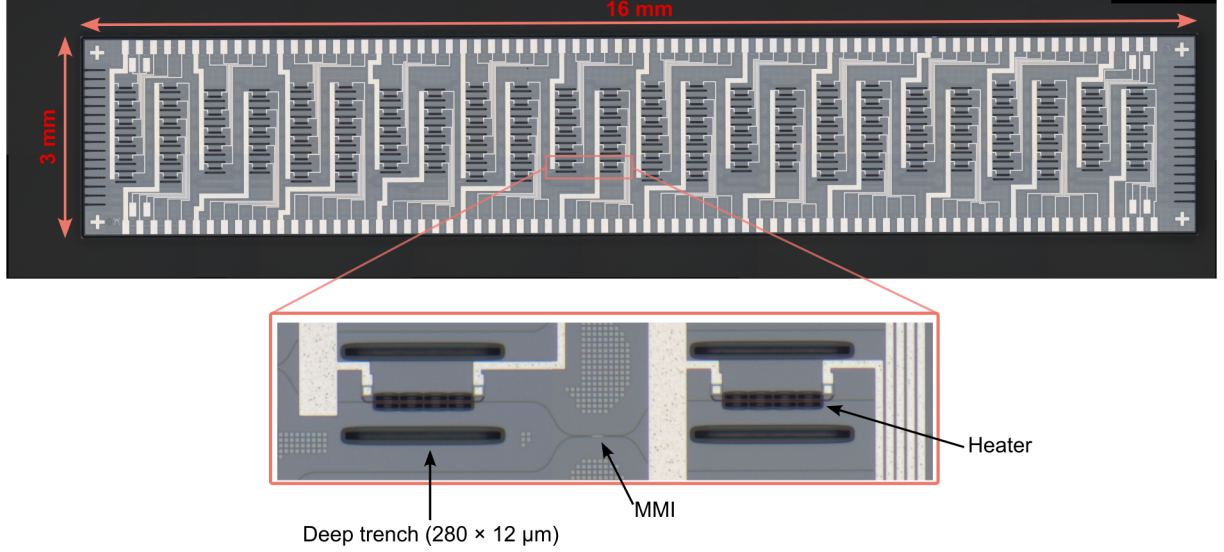


Fig. S2. Photonic chip. Optical microscope image of the programmable photonic processor. The chip measures 16×3 mm and integrates 264 elements (phase shifters and MMIs). Deep trenches ($280 \times 12 \mu\text{m}$) are etched around the Mach-Zehnder interferometers to reduce thermal crosstalk between neighboring heaters. Inset: magnified view highlighting an MMI, a thermo-optic heater, and surrounding trenches.

S4. Extended simulation of seven-site transport

To extend the main-text results, we simulate the seven-site hexagon over a longer evolution window of $9T$, see Fig. S3. This allows us to confirm that the directional transport is not a short-time artifact but persists across multiple cycles. In this regime, the circulating multi-peak/single-peak structure executes more than one full rotation around the perimeter, demonstrating sustained chiral motion.

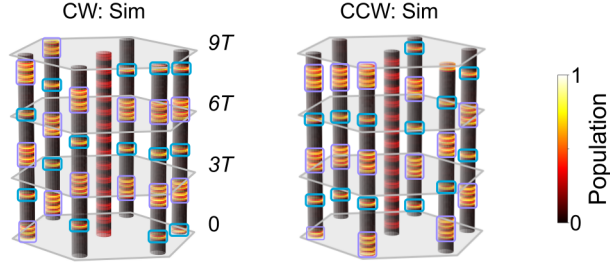


Fig. S3. Extended seven-site dynamics. Simulated evolution under CW (left) and CCW (right) drives at the gap-optimized period $T = 13.6647$, using 15 steps per period. Horizontal planes mark $0, 3T, 6T, 9T$. The characteristic multi-peak/single-peak pattern described in the main text persists over long times, advancing chirally around the perimeter and completing on the order of two full rotations. Violet boxes mark the multi-peak packet and cyan boxes mark the single-peak packet; for clarity, arrows used in the main-text are omitted here.